2023 IEEE Workshop on Electrical Machines Design, Control and Diagnosis (WEMDCD) | 978-1-6654-8693-4/23/$31.00 ©2023 IEEE | DOI: 10.1109/WEMDCD55819.2023.10110935

Design Morphology for High-Speed Rotors in Electrical Machines Based on Analytical Models

Maximilian Lauerburg, Polkrit Toraktrakul and Kay Hameyer
Institute of Electrical Machines (IEM)
RWTH Aachen University
Aachen, Germany
maximilian.lauerburg@iem.rwth-aachen.de

***Abstract*—The state-of-the-art for high-speed rotors in induction machines and permanent magnet synchronous machines is discussed. The rotors for permanent magnet synchronous machines are distinguished between rotors with surface permanent magnets and rotors with buried permanent magnets. For induction machines, the conventional laminated rotor is compared to solid rotor designs. Based on the equivalent ring method, analytical models to calculate mechanical stresses within the presented rotor topologies are developed. Thereby a morphological comparison of the rotor topologies with regard to achievable circumferential velocity is possible.**

***Index Terms*—High-speed electrical machines, Design morphology, Equivalent ring method.**

I. Comparison of State-Of-The-Art High-Speed Electrical Machines

One of the limiting factors of high-speed operation are large mechanical stresses in the rotor. The circumferential velocity v_c at the outer rotor radius r_rotor sets the dimension of the rotor in relation to the rotational speed n. Therefore v_c is often used as the reference dimension for high-speed operation (1). Since the circumferential velocity directly correlates with the mechanical stresses, it represents the mechanical rigidity of the rotor structure. Rotors exceeding 100 m/s are considered as high-speed designs [1].

$$v_\mathrm{c} = 2\pi \frac{n}{60} \cdot r_\mathrm{rotor} \tag{1}$$

As the rotational speed increases, the losses within the electrical machine increase as well. These losses can be caused by electromagnetics and mechanics. Increased losses lead to excessive heat which has to be extracted by the cooling system in order to avoid thermal failure of components. Consequently, the achievable rotational speed is limited by several constraints [1], [2].

Different topologies of high-speed electrical machines are often compared in diagrams showing the achievable mechanical power at maximum rotational speed. However, the mechanical rigidity of the rotor topologies can not so easily be benchmarked with these dimensions.

Permanent magnet synchronous machines (PMSM) and induction machines (IM) are the most promising topologies for high-speed operation [1], [3]. For PMSM, surface permanent magnets (SPMSM), which are retained by a sleeve, are compared to buried permanent magnets (IPMSM) (Fig. 1).

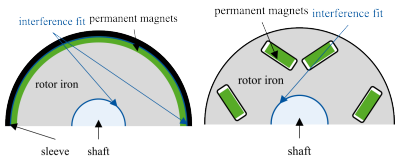

(a) SPMSM (b) IPMSM

Fig. 1. Respected rotor cross-sections for PMSM. (a) The permanent magnets are secured with a sleeve. (b) Permanent magnets are buried in lamination sheet.

IM are distinguished between standard laminated rotor designs (Laminated IM) and solid rotor designs (Solid IM). In all solid rotor configurations, the rotor iron and the shaft are made of one solid body in order to achieve maximum mechanical strength [4], [5]. In case of a Solid IM, the squirrel cage can be constructed by either cutting slots in the rotor iron, coating the rotor with a copper alloy or inserting bars into the iron. The coated solid rotor and the design with rotor bars are shown in Fig. 2.

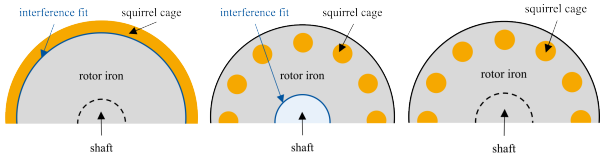

(a) Solid Rotor IM (b) Laminated IM (c) Solid Rotor IM

Fig. 2. Compared rotor cross-sections for IM. The rotor iron and the shaft are made of one solid body in (a) and (c). A standard laminated design is shown in (b).

In [6] the concept of holding bands within the rotor is presented. The properties of the outer holding band (OHB), the ring between the rotor surface and the closest adjacent cavity in the rotor cross section, is restricting the achievable circumferential velocity. For SPMSM, the outer holding band is equal to the retaining sleeve, which secures the surface magnets against the centrifugal forces. For IPMSM and Laminated IM the outer holding band is a circular section of the lamination sheets. The OHB is limited from the inside by the outermost contour of the cavities, which are accommodating the permanenent magnets or the rotor bars. The outer holding band for Solid IM is dependent on the squirrel cage design.

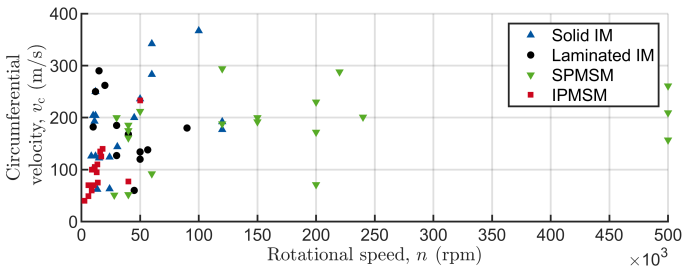

Fig. 3. Comparison of machine topologies with respect to circumferential velocity at maximum rotational speed based on machine designs in [1], [3] and [7] - [18].

Finally, the machine topologies are benchmarked with respect to circumferential velocity and rotational speed in Fig. 3, so that it is possible to compare the mechanical strength.

The Solid IM achieves the highest circumferential velocity and therefore has the highest mechanical rigidity, followed by the SPMSM and Laminated IM. In comparison, the IPMSM has the lowest mechanical strength. Nevertheless, the maximum of the rotational speed can be noticed for SPMSM, although SPMSM seems to have a lower mechanical strength than the Solid IM.

A general approach for calculating mechanical stresses in the discussed rotor topologies is developed. Hence, it is possible to evaluate the influence of the dimensions of each rotor topology in a morphological comparison on rotor strength. Salient pole rotors are not considered as these are comparatively less suitable for high-speed operation. All respected rotor topologies have a closed OHB.

II. Equivalent Ring Method and Validation

A. Introduction of Method to Analytically Calculate Mechanical Stresses in Rotors

At the beginning of the design process for high-speed electrical machines, the mechanical strength of the rotor has to be ensured by mechanical simulations. In order to reduce the simulation effort, various methods have been presented in literature to analytically calculate the mechanical stresses in critical areas within the rotor. Methods to calculate the mechanical stresses in magnet bridges of IPMSM are shown in [19] – [21]. Methods are presented to calculate mechanical stresses at the inner contour of retaining sleeves for SPMSM in [19], [22] and [23].

The mentioned methods have in common that they are focusing on PMSM. A general approach for calculating the achievable circumferential velocity of all considered rotor topologies in PMSM and IM (Fig. 1 and Fig. 2), taking into consideration the effects of centrifugal forces as well as press fits, is presented in this paper.

The concept is developed based on the Equivalent Ring Method (ERM), which is introduced in [19]. The ERM transforms the centrifugal forces acting on the mechanical weak links in the rotor, the magnet bridges in IPMSM, into an equivalent ring with artificially increased mass density. The dimensions of this equivalent ring are based on the OHB within the rotor.

However, the models for IPMSM discussed in literature neclect the influence of the pressfit on the stresses in the magnet bridges [19] - [21]. Therefore, the total mechanical stress σ_{total} at a defined point consists of the stress $\sigma_{\mathrm{centrifugal}}$ due to centrifugal forces and the stress $\sigma_{\mathrm{pressfit}}$, as a result of a pressfit imposing additional load to the rotor materials (2).

$$\sigma_{\mathrm{total}} = \sigma_{\mathrm{centrifugal}} + \sigma_{\mathrm{pressfit}} \tag{2}$$

Since an OHB can also be identified in the other rotor topologies compared to IPMSM, the ERM is generalized in order to calculate the stresses $\sigma_{\mathrm{centrifugal}}$. A method to evaluate stresses due to pressfits completes the stress calculation $\sigma_{\mathrm{pressfit}}$ and enables the morphological comparison.

B. Mechanical Simulations

Rotors for SPMSM and Laminated IM were constructed and burst tests were performed in [9]. The deformation of the rotor surface was measured during ramp-up of rotational speed. The burst speed for both rotors has been determined. In addition, mechanical simulations in ANSYS of both rotors correlate with measurements of rotor deformation and burst speed.

The setup of the mechanical simulations was shown in detail: material properties, contact definition and additional boundary conditions [9]. The same setup in ANSYS was adopted for the mechanical simulations used to develop the dependencies for the achievable circumferential velocity.

III. Analytical Calculation of Mechanical Stress in Topologies

A. Influence of Pressfits on Maximum Stress

Pressfits are required within rotors of electrical machines to secure components against relative movement and to transfer torque. Depending on the rotor topology, pressfits are used at different locations. For IPMSM and Laminated IM, the rotor iron has to be joined on a shaft. In case of Solid IM, the shaft and the rotor iron are one component. A sleeve is pressfitted on top of the rotor in SPMSM and copper coated solid rotor designs.

The interference fit imposes additional forces in the rotor. Since the pressfits can be located at different locations within a rotor topology, the influence on the achievable circumferential velocity is topology dependent. An approach is developed to consider these additional stresses in rotors of high-speed electrical machines. In [24] design rules for cylindrical pressfits under centrifugal load are shown. However, these rules are solely valid when the shaft and the hub consist of the same material and the shaft has no bore. Therefore these dependencies are developed further in order to be applicable for rotors in electrical machines.

The pressure at standstill p_0 in the pressfit can be determined with (3). r_{b} is the bore radius of the shaft, r_{f} is the gap

diameter of the pressfit, δ is the interference and E_{equiv} is the homogenized Youngs modulus.

$$p_0 = \sqrt{1 - \frac{r_\mathrm{b}}{r_\mathrm{f}}} \cdot \frac{1 - (\frac{r_\mathrm{f}}{r_\mathrm{rotor}})^2}{2} E_{\mathrm{equiv}} \frac{\delta}{2r_\mathrm{f}} \tag{3}$$

The homogenization is equal to the sum of the material parameters which are weighed by the area share in the press-fit. The pressure p reduces with increasing rotational speed according to [24], since the hub expands more than the shaft and therefore the interference decreases (4).

$$p = p_0 \cdot [1 - (\frac{2\pi r_\mathrm{rotor} n}{v_\mathrm{lift}})^2] \tag{4}$$

v_lift is the circumferential velocity where the lamination sheet lifts off the shaft at zero interference fit (5). χ is a parameter which considers the material pairing and the dimensional ratio of r_rotor, r_f and r_b. ν_{equiv} is the homogenized Poissons ratio.

$$v_\mathrm{lift} = 2 \cdot \sqrt{\frac{E_{\mathrm{equiv}} \cdot (\frac{\delta}{2r_\mathrm{f}})\chi}{\rho_{\mathrm{equiv}}[(1-\nu_{\mathrm{equiv}})(\frac{r_\mathrm{f}}{r_\mathrm{rotor}})^2 + 3 + \nu_{\mathrm{equiv}}]}} \tag{5}$$

The stress in the hub can be evaluated with (6) in relation to the distance to the gap radius r_f. r_σ is equal to the radius where the maximum stress due to centrifugal forces occurs within the rotor cross-section. η considers the properties of the cavities between the pressfit and the OHB, since these influence the transfer of stress in the rotor.

$$\sigma_{\mathrm{pressfit}}(r_\sigma) = p \cdot \eta \cdot \Omega(r_\sigma) \tag{6}$$

The term (7) considers the relative position of the point with maximum centrifugal stress r_σ to the gap radius r_f. Ω reaches maximum when the point of maximum centrifugal stress meets with the gap radius.

$$\Omega(r_\sigma) = \frac{(\frac{r_\mathrm{f}}{r_\sigma})^2 + (\frac{r_\mathrm{f}}{r_\mathrm{rotor}})^2}{1 - (\frac{r_\mathrm{f}}{r_\mathrm{rotor}})^2} \tag{7}$$

B. IPMSM

Permanent magnets arranged tangentially to the rotor surface are chosen for the IPMSM reference geometry. The area of the lamination sheet A_Fe which is loading the magnet bridges is minimized and the stresses is reduced [20]. The basic rotor arrangement can be seen in Fig. 4.

The equivalent density ρ_{equiv} of the ring is determined according to (8) where ρ_Fe is the density of the lamination sheet, ρ_PM is the density of the permanent magnets, A_Fe the area of the lamination sheet which loads the magnet bridges, A_PM the area of one permanent magnet and A_{equiv} the respected area of the OHB.

$$\rho_{\mathrm{equiv}} = \frac{\rho_\mathrm{Fe} + \rho_\mathrm{PM}}{2} \cdot \frac{A_\mathrm{Fe} + A_\mathrm{PM}}{A_{\mathrm{equiv}}} \tag{8}$$

The equivalent stress σ_{equiv} in the magnet bridge can be calculated according to (9) where r_rotor is the outer rotor radius, $r_{\mathrm{i,equiv}}$ is the radius of the inner contour of the OHB and n is the rotational speed.

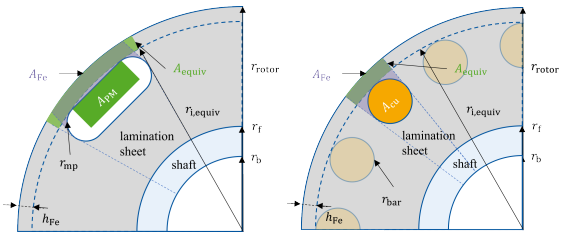

(a) IPMSM (b) Laminated IM

Fig. 4. Respected areas and dimensions in IPMSM and IM rotor cross-section for mechanical stress calculation.

$$\sigma_{\mathrm{equiv}} = (\frac{r_\mathrm{rotor} + r_{\mathrm{i,equiv}}}{2})^2 \cdot (2\pi n)^2 \cdot \rho_{\mathrm{equiv}} \tag{9}$$

The maximum stress $\sigma_{\mathrm{max,centrifugal}}$ at the magnet pocket contour facing towards the OHB can be determined by the stress concentration factor K_t according to (10).

$$\sigma_{\mathrm{max,centrifugal}} = K_{\mathrm{t,IPMSM}} \cdot \sigma_{\mathrm{equiv}} \tag{10}$$

The stress concentration factor for IPMSM is given by (11), which is developed based on a factor given in [25]. h_Fe is equal to the thickness of the OHB, r_mp the radius of the magnet pocket facing towards the OHB.

$$K_{\mathrm{t,IPMSM}} = \frac{0.9 \sqrt[3]{\frac{r_\mathrm{rotor}}{h_\mathrm{Fe}}} \cdot (\frac{h_\mathrm{Fe}}{r_\mathrm{mp}} + 1) \cdot \sqrt{\frac{h_\mathrm{Fe}}{r_\mathrm{mp}}}}{\sqrt{\frac{h_\mathrm{Fe}}{r_\mathrm{mp}}} + \arctan(\sqrt{\frac{h_\mathrm{Fe}}{r_\mathrm{mp}}}) \cdot (\frac{h_\mathrm{Fe}}{r_\mathrm{mp}} + 1)} \tag{11}$$

The influence of the pressfit between the lamination package and the shaft is superimposed. All in all, the achievable circumferential velocity of IPMSM v_c can now be determined when σ_total is equal to the yield strength of the material used for the lamination sheet R_p.

$$v_\mathrm{c} = \sqrt{\frac{R_\mathrm{p} - \eta\Omega \cdot p_0}{K_{\mathrm{t,IPMSM}} \cdot (\frac{r_\mathrm{rotor} + r_{\mathrm{i,equiv}}}{2r_\mathrm{rotor}})^2 \cdot \rho_{\mathrm{equiv}} - \frac{1}{v_\mathrm{lift}^2}\eta\Omega \cdot p_0}} \tag{12}$$

Where Ω is evaluated for the orbit of the inner contour of the OHB $r_{\mathrm{i,equiv}}$, which is equal to the position of the maximum stress at the magnet pocket contour (13).

$$\Omega(r_\sigma = r_{\mathrm{i,equiv}}) = \frac{(\frac{r_\mathrm{f}}{r_{\mathrm{i,equiv}}})^2 + (\frac{r_\mathrm{f}}{r_\mathrm{rotor}})^2}{1 - (\frac{r_\mathrm{f}}{r_\mathrm{rotor}})^2} \tag{13}$$

The mechanical stress in the magnet bridge is evaluated along a path that perpendicularly intersects the isolines of the mechanical stresses. The stress in the magnet bridge mainly consists of tensile stress. The share of tensile stress increases with decreasing distance to the magnet pocket contour [21].

The formulas of the shown analytical model are developed to match the largest stress at the magnet pocket contour. In Fig. 5 the comparison of FE Simulation and the model is

shown with regard to the achievable circumferential velocity when the stress at the pocket contour reaches the materials yield strength limit. In this diagram the radius of the pocket contour as well as the thickness of the OHB have been varied. The model is in agreement with the performed mechanical simualtions in ANSYS, based on the constraints shown in [9].

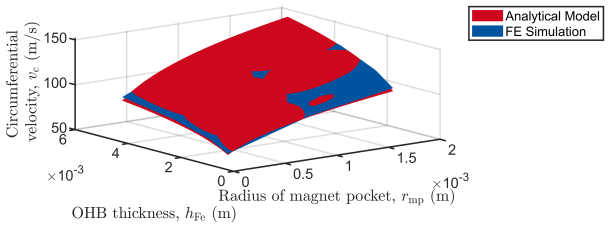

Fig. 5. Comparison of analytical model for IPMSM with FE simulation in ANSYS with respect to achievable circumferential velocity.

C. SPMSM

In SPMSM, the surface permanent magnets have to be secured against centrifugal forces with a sleeve. The sleeve is pressfitted on top of the rotor. The geometry of the sleeve is equal to the OHB. The radius of the inner contour of the OHB $r_{\mathrm{i,equiv}}$ meets with the gap radius r_{f} of the pressfit at the inner contour of the retaining sleeve. The maximum stress due to centrifugal forces in rotor cross section of SPMSM can be found at the inner contour of the retaining sleeve [19], [23] and [26].

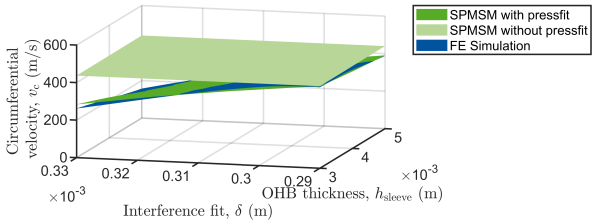

Fig. 6. Influence of pressfit in SPMSM on achievable circumferential velocity with regard to interference fit and sleeve thickness. Comparison of analytical model with FE simulation based on SPMSM with pressfit.

Analytical formulas for calculating radial and tangential stresses in a rotating hollow disc were published in [27]. The maximum stress at the inner contour in a retaining sleeve can be calculated with (14). ν and ρ are the Poissons ratio and the density of the sleeve material.

$$\sigma_{\mathrm{max,centrifugal}} = \frac{3+\nu}{4}\rho(2\pi n)^2(r_{\mathrm{rotor}}^2 + \frac{1-\nu}{3+\nu}r_{\mathrm{f}}^2) \quad (14)$$

r_{f} is the bore radius of the sleeve and is equal to the gap radius as the sleeve is pressfitted on top of the permanent magnets. Therefore, r_{f} is equal to the radius of the inner contour of the OHB $r_{\mathrm{i,equiv}}$.

$$v_{\mathrm{c}} = \sqrt{\frac{R_{\mathrm{p}} - \eta\Omega \cdot p_0}{4\rho \cdot ((1-\nu)(\frac{r_{\mathrm{i,equiv}}}{r_{\mathrm{rotor}}})^2 + 3 + \nu) - \frac{1}{v_{\mathrm{lift}}^2}\eta\Omega \cdot p_0}} \quad (15)$$

The term Ω for the pressfit is then evaluated for r_{f}, since the point of the largest stress due to centrifugal forces meets with the gap radius of the pressfit. Consequently, the influence of the pressfit in SPMSM is larger than in IPMSM with regard to achievable circumferential velocity (15) and (16).

$$\Omega(r_\sigma = r_{\mathrm{f}}) = \frac{1 + (\frac{r_{\mathrm{f}}}{r_{\mathrm{rotor}}})^2}{1 - (\frac{r_{\mathrm{f}}}{r_{\mathrm{rotor}}})^2} \quad (16)$$

In Fig. 6 the influence of the pressfit on the achievable circumferential velocity of SPMSM is shown. The effective circumferential velocity, which can be reached practically, gets reduced with increasing interference δ between permanent magnets and sleeve. The analytical model shows good agreement with the FE simulation (Fig. 6).

D. Laminated IM

The shapes of slots and rotor bars for squirrel cages in IM vary according to the requirements [2]. A uniform stress distribution is preferred in high-speed operation. Closed slot openings are advantageous for high mechanical strength [4]. Consequently, the rotor bar cross-section is chosen to be circular and the OHB is closed (Fig. 4).

The rotor bars are placed as close as possible to the main air gap from electromagnetic view [2]. However, small OHB are limiting the achievable circumferential velocity, so a trade-off must be found. The principle of ERM is applied on the respected rotor cross-section according to the area definition shown in Fig. 4. The equivalent ring is assumed with an equivalent density based on (8) with respect to the properties of the rotor bar.

The formula to determine the equivalent stress σ_{equiv} is consistent to IPMSM (9). The largest stresses in the OHB of an IM can be found at the rotor surface [9]. The stress concentration due to the bar shape and the thickness of the OHB can be determined with (17). The maximum stress in the OHB can then be determined with (10).

$$K_{\mathrm{t,IM}} = 1.2 \cdot \exp(-(\frac{\frac{h_{\mathrm{Fe}}}{r_{\mathrm{bar}}} - 0.3}{0.7})^2) \cdot [0.06 + 3 \cdot \frac{h_{\mathrm{Fe}}}{r_{\mathrm{bar}}}] \quad (17)$$

Due to the fact that the stress concentration effect of $K_{\mathrm{t,IM}}$ is lower than in $K_{\mathrm{t,IPMSM}}$, the achievable circumferential velocities of IM are not exclusively limited by the propterties of the OHB. The stresses in the OHB and at the bore contour of the lamination sheet must be evaluated. The stress due to centrifugal forces at the bore contour of the lamination sheet can be evaluated with (14). The resulting achievable circumferential velocity of IM, under consideration of the pressfit, is now the minimum of two expressions. $v_{\mathrm{c,1}}$ is evaluating the stress in the OHB and $v_{\mathrm{c,2}}$ is evaluating the stress at the bore contour of the lamination sheet. $v_{\mathrm{c,1}}$ is given by (18).

$$v_{\mathrm{c,1}} = \sqrt{\frac{R_{\mathrm{p}} - \eta\Omega \cdot p_0}{K_{\mathrm{t,IM}} \cdot (\frac{r_{\mathrm{rotor}} + r_{\mathrm{i,equiv}}}{2r_{\mathrm{rotor}}})^2 \cdot \rho_{\mathrm{equiv}} - \frac{1}{v_{\mathrm{lift}}^2}\eta\Omega \cdot p_0}} \quad (18)$$

Where Ω is evaluated for the orbit of the outer rotor radius r_{rotor}, as it is equal to the position of the maximum stress at the pocket contour (19).

$$\Omega(r_\sigma = r_{\mathrm{rotor}}) = \frac{2(\frac{r_\mathrm{f}}{r_{\mathrm{rotor}}})^2}{1-(\frac{r_\mathrm{f}}{r_{\mathrm{rotor}}})^2} \tag{19}$$

$v_{\mathrm{c},2}$ can be determined with (15) and (16), however r_f is not equal to $r_{\mathrm{i,equiv}}$ in contrast to SPMSM. The technical possible circumferential velocity is then given by (20).

$$v_\mathrm{c} = \min(v_{\mathrm{c},1}, v_{\mathrm{c},2}) \tag{20}$$

In Fig. 7 the evaluating process for the effective achievable circumferential velocity v_c and the comparison with the FE simulation are shown.

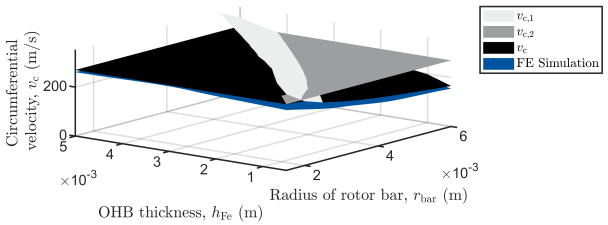

Fig. 7. The total achievable circumferential velocity of IM v_c is the minimum of the achievable circumferential velocities with regard to OHB $v_{\mathrm{c},1}$ and the bore contour $v_{\mathrm{c},2}$. Comparison of analytical model with FE simulation with regard to overall achievable circumferential velocity.

By exclusively focussing on the stresses in the OHB, the stresses can be reduced by the burial depth of the rotor bars. However, these potential high circumferential velocities can technically not be used, as the stress at the bore contour becomes to large.

E. Solid IM

Different designs of solid rotor induction machines have been introduced in [4] and [5]. In case of a solid rotor with discrete number of rotor bars, there is no pressfit in the rotor (Fig. 2). For such solid rotor design, the achievable circumferential velocity can be determined with the presented method for laminated IM (18), with the constraint that the interference δ is zero. However, $v_{\mathrm{c},2}$ is based on a rotating full disc, since in most solid rotor designs there is no bore found in the shaft [4], [5]. Due to the relatively lower notch effect of the cavities for the rotor bars, the maximum circumferential velocity is also restricted by the stresses in the center of the rotor (21).

$$v_{\mathrm{c},2} = \sqrt{\frac{8 \cdot R_\mathrm{p}}{\rho \cdot (3+\nu)}} \tag{21}$$

A copper coated design, shown in Fig. 2, can be evaluated with the presented method for SPMSM, due to the fact that the rotor structure is comparable. As the specific yield strength R_p/ρ of copper alloys is comparatively lower than those of steel alloys, it is reasonable that the copper coated solid rotor design does not have the best potential for high-speed operation. Consequently, a solid rotor design with a descrete number of rotor bars is used for the morphological comparison. In [28] different materials for the rotor iron of solid rotor IM have been compared with regard to mechanical and electromagnetic behavior. Imacro M, which has a yield strength of 700MPa, is suggested and therefore used for the comparison.

IV. Morphological Comparison of Rotor Topologies

Based on (20), (12) and (15) the general dependency of the circumferential velocity can be derived (22).

$$v_\mathrm{c} \propto \sqrt{\frac{R_\mathrm{p} - (\frac{r_\mathrm{f}}{r_\sigma})^2 \cdot E\frac{\delta}{r_\mathrm{f}}}{K_\mathrm{t} \cdot \rho - (\frac{r_\mathrm{f}}{r_\sigma})^2 \cdot \frac{1}{v_{\mathrm{lift}}^2} E\frac{\delta}{r_\mathrm{f}}}} \tag{22}$$

The specific yield strength R_p/ρ of the material used for the OHB has the biggest impact on the achievable circumferential velocity. Stress concentration at cavities within the rotor reduces the circumferential velocity with K_t. The influence of the pressfit on the achievable circumferential velocity increases when the radius to the area of maximum centrifugal load r_σ is close to the gap radius r_f. Also high interferences δ are reducing the achievable circumferential velocities v_c.

The mechanical properties of the rotor materials used for the OHB are listed in Tab. I. The highest specific yield strength can be recognized for the retaining sleeve material in SPMSM, followed by Imacro M used for the solid rotor design.

TABLE I
Comparison of Material Properties

Rotor Topology	***IPMSM Laminated IM***	***Solid IM***	***SPMSM***
OHB Material	***M250-35A [29]***	***4CrMn16-4 [30]***	***Ti6A14V [31]***
ρ in $\mathrm{kg/m^3}$	7600	7800	4400
R_p in MPa	455	700	825
R_p/ρ in $(\mathrm{m/s})^2$	$59.8 \cdot 10^3$	$89.7 \cdot 10^3$	$187.5 \cdot 10^3$

All considered rotor topologies are compared in Fig. 8 for different thicknesses h of the OHB and different radius r of the cavity facing towards the OHB. The achievable circumferential velocities without pressfits are shown for Laminated IM, IPMSM and SPMSM, so that the reducing influence of the interference fit can be quantified. For these rotor topologies, a pressfit is technically needed, hence the usable circumferential velocity is reduced. The considered Solid IM design has no need for a pressfit.

Due to the highest stress concentration effect in rotors of IPMSM, buried permanent magnets allow the lowest circumferential velocity with respect to the thickness of the OHB and the radius of the cavity. The notch effect is comparatively larger, since the cavities for the permanent magnets are usually larger than those used for rotor bars [4], [16].

The achievable circumferential velocity of the laminated IM increases when the bars are buried deeper into the rotor.

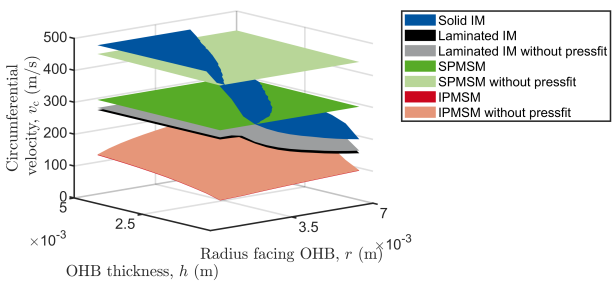

Fig. 8. Comparison of rotor topologies with regard to achievable circumferential velocity in dependence on the thicknees h of the OHB and the radius r of the cavity facing towards the OHB.

However, the maximum circumferential velocity is limited by the stresses at the bore contour for the shaft. The impact of the pressfit in SPMSM is at its largest as the point of the maximum centrifugal stress meets with the gap radius at the inner contour of the retaining sleeve (Fig. 8). Therefore the highest specific yield strength of the materials R_p/ρ used in the comparison does not translate to the highest circumferential velocity (22).

The Solid IM achieves higher circumferential velocities than the laminated IM, due to the used material for the rotor iron, the absence of pressfits as well as the absence of bore in the shaft. The solid structure largely reduces stresses in the rotor and therefore enables the highest circumferential velocities [27].

V. Conclusion

The presented design morphology enables the evaluation of the dimensions of the presented rotor topologies on achievable circumferential velocity and thereby rotor strength. The influence of the geometry parameters can be evaluated separately, so that the limitations for a rotor topology can be compared analytically with respected topologies. The applicability of the methodology to other rotor topologies such as synchronous reluctance machines is to be investigated further.

References

[1] A. Binder and T. Schneider, “High-Speed Inverter-Fed AC Drives”, International Aegean Conference on Electrical Machines and Power Electronics, IEEE, 2007.

[2] J. Pyrhönen, T. Jokinen and V. Hrabovacava, “Design of rotating electrical machines”, John Wiley and Sons, vol. 2, 2013.

[3] D. Gerada, A. Mebarki, N. L. Brown, C. Gerada, A. Cavagnino and A. Boglietti, “High-Speed Electrical Machines: Technologies, Trends and Developments”, IEEE Transactions on Industrial Electronics, vol. 61, 2014.

[4] T. Mauffrey, J.-F. Pradurat, L. Durantay and J. Fontini, “Comparison of 5 Different Squirrel Cage Rotor Designs for Large High Speed Induction Motors”, PCIC Europe, IEEE, 2013.

[5] T. Aho, “Electromagnetic Design of a Solid Steel Rotor Motor for Demanding Operation Environments”, Dissertation at Lappeenranta University of Technology, 2007.

[6] B. Groschup and F. Leonardi, “Combined electromagnetic and static structural simulation to reduce the weight of a Permanent Magnet machine rotor for HEV application”, IEEE International Electric Machines and Drives Conference, 2017.

[7] L. Papini, C. Gerade, D. Gerade and A. Mebarki, “High Speed Solid rotor Induction Machine: Analysis and Performances”, International Conference on Electrical Machines and Systems, IEEE, 2014.

[8] J. Barta, C. Ondrusek, P. Losak and R. Vlach, “Design of High-Speed Induction Machine for the 6 kW 120000 rpm Helium Turbo-Circulator”, International Conference on Electrical Machines, 2016.

[9] M. Gerlach, M. Zajonc and B. Ponick, “Mechanical stress and deformation in the rotors of a high-speed PMSM and IM”, Journal e & i Elektrotechnik und Informationstechnik, 2021.

[10] R. Thomas, H. Husson, L. Garbuio and L. Gerbaud, “Comparative study of the Tesla Model S and Audi e-Tron Induction Motors”, Conference on Electrical Machines, Drives and Power Systems, IEEE, 2021.

[11] J. Saari, “Thermal Analysis of High-speed Induction Machines”, Finnish Academy of Technology, Dissertation at Helsinki University of Technology, 1998.

[12] A. Binder, T. Schneider and M. Klohr, “Losses in High-Speed Permanent Magnet Motor with Magnetic Levitation for 40000 rpm/40 kW”, International Conference on Electrical Machines, 2004.

[13] P. Lück, K. Bennewitz and J. Tousen, “Volkswagen’s electric drivetrains of the new modular e-drive kit (MEB)”, International VDI Congress, VDI-Berichte Nr. 2354, pp. 517–530, 2019.

[14] A. Tüysüz, C. Zwyssig and J.W. Kolar, “A Novel Motor Topology for High-Speed Micro-Machining Applications”, IEEE Transactions on Industrial Electronics, 2014.

[15] F. Ismagilov, V. Vavilov and D. Gusakov, “High-Speed Electric Machine with a Speed of 1.2 million rpm”, International Symposium on Power Electronics, Electrical Drives, Automation and Motion, IEEE, 2018.

[16] A. Krings and C. Monissen, “Review and Trends in Electric Traction Motors for Battery Electric and Hybrid Vehicles”, International Conference on Electrical Machines, IEEE, 2020.

[17] C. Goli, M. Manjrekar, S. Essakiappan, P. Sahu and N. Shah, “Landscaping and Review of Traction Motors for Electric Vehicle Applications”, IEEE Transportation Electrification Conference & Expo , 2021.

[18] T. Burress, “Electrical Performance, Reliability Analysis, and Characterization”, Oak Ridge National Laboratory, National Transportation Research Center, 2017.

[19] A. Binder and T. Schneider, “Fixation of Buried and Surface-Mounted Mangets in High-Speed Permanent-Magnet Synchronous Machines”, Industry Applications Conference, IEEE, 2006.

[20] C. Feng, L. Yi, L. Peixin and P. Yulong, “Caluclation of the Maximum Mechanical Stress on the Rotor of Interior Permanent-Magnet Synchronous Motors”, IEEE Transactions on Industry Applications, 2016.

[21] G. Chu, M. F. Rahman and B. Sarlioglu, “Analytical Calculation of Maximum Mechanical Stress on the Rotor of Interior Permanent-Magnet Synchronous Machines”, IEEE Transactions on Industry Applications, 2020.

[22] D. J. B. Smith, “High speed High Power Electrical Machines”, Dissertation at Newcastle University, 2014.

[23] L. Chen and C. Zhu, “Rotor Strength Analysis for High Speed Permaent Magnet Machines”, International Conference on Electrical Machines and Systems, IEEE, 2014.

[24] Interference fits - Part 1: Calculation and design rules for cylindrical self-locking pressfits, DIN 7190-1, 2017.

[25] W. D. Pilkey and D. F. Pilkey, “Peterson’s Stress Concentration Factors”, John Wiley & Sons, 2008.

[26] F. Zhang, G. Du, T. Wang, G. Liu and W. Cao, “Rotor Retaining Sleeve Design for a 1.12-MW High-Speed PM Machine”, IEEE Transactions on Industry Applications, 2015.

[27] B. Bender and D. Göhlich, “Dubbel Band 1 - Taschenbuch für den Maschinenbau”, P. 434, Springer Verlag, 2020.

[28] P. Lindh, P. Immonen, C. Di, M. Degano and J. Pyrhönen, “Solid-Rotor Material Selection for Squirrel-Cage High-Speed Solid-Rotor Induction Machine”, Conference of the IEEE Industrial Electronics Society, 2019.

[29] Cogent Surahammars Bruks AB (2008): Typical data for SURA M250-35A. https://www.tatasteeleurope.com/automotive/products/electrical-steel [26.11.2022]

[30] Steel Navigator (2022): Typical data for Imacro M. https://steelnavigator.ovako.com/steel-grades/4crmn16-4/ [26.11.2022]

[31] H. Fang, R. Qu, J. Li, P. Zheng and X. Fan, “Rotor Design for High-Speed High-Power Permanent-Magnet Synchronous Machines”, IEEE Transactions on Industry Applications, 2017.